COMMUNICATIONS IN NUMERICAL METHODS IN ENGINEERING
Commun. Numer. Meth. Engng 2008; **24**:1781–1804
Published online 19 November 2007 in Wiley InterScience (www.interscience.wiley.com). DOI: 10.1002/cnm.1066

Analysis of rubber-like materials using meshless local Petrov–Galerkin (MLPG) method

R. C. Batra[1] and M. Porfiri[2,*,†]

[1]*Department of Engineering Science and Mechanics, Virginia Polytechnic Institute and State University, Blacksburg, VA 24061, U.S.A.*
[2]*Department of Mechanical, Aerospace and Manufacturing Engineering, Polytechnic University, Brooklyn, NY 11201, U.S.A.*

SUMMARY

Large deformations of rubber-like materials are analyzed by the meshless local Petrov–Galerkin (MLPG) method. The method does not require shadow elements or a background mesh and therefore avoids mesh distortion difficulties in large deformation problems. Basis functions for approximating the trial solution and test functions are generated by the moving least-squares (MLS) method. A local mixed total Lagrangian weak formulation of non-linear elastic problems is presented. The deformation gradient is split into deviatoric and dilatational parts. The strain energy density is expressed as the sum of two functions: one is a function of deviatoric strains and the other is a function of dilatational strains. The incompressibility or near incompressibility constraint is accounted for by introducing the pressure field and penalizing the part of the strain energy density depending upon the dilatational strains. Unlike in the mixed finite element formulation, in the MLPG method there is no need for different sets of basis functions for displacement and pressure fields. Results computed with the MLPG method for a few sample problems are found to compare very well with the corresponding analytical solutions. Copyright © 2007 John Wiley & Sons, Ltd.

Received 21 January 2007; Revised 23 September 2007; Accepted 8 October 2007

KEY WORDS: finite deformations; rubber-like materials; Petrov–Galerkin; meshless method; locking phenomenon

*Correspondence to: M. Porfiri, Department of Mechanical, Aerospace and Manufacturing Engineering, Polytechnic University, Brooklyn, NY 11201, U.S.A.
†E-mail: mporfiri@poly.edu

Contract/grant sponsor: Office of Naval Research; contract/grant numbers: N00014-07-1-0419, N00014-06-1-0567

1. INTRODUCTION

Rubber-like materials are frequently used in the automotive industry, mechanical, civil, electrical and electronic engineering, see, e.g. [1]. Biological tissues can also be regarded as rubber-like materials. For example, the material of an arterial wall [2] is modeled as rubber-like.

In continuum mechanics, rubber-like solids are generally modeled as isotropic, incompressible and hyperelastic. From a theoretical point of view, the incompressibility constraint facilitates finding analytical solutions for isotropic hyperelastic problems, see, for example, [2]. Besides homogeneous deformations, there are five families of inhomogeneous deformations [3] that can be produced in every incompressible isotropic hyperelastic solid. Some works have investigated the possibility of treating rubber as a nearly incompressible material by separating the strain energy for distortional deformations from that for the dilatational ones using Penn's invariants [4] and the multiplicative decomposition of the deformation gradient into a volume preserving deformation and a pure dilatation, see, e.g. [5]. In [6] it is proved that the behavior of slightly compressible materials may approximate well that of incompressible materials.

The analysis of problems for rubber-like materials is a challenging task in computational mechanics due to the possibility of extremely large deformations and the nearly incompressible or genuinely incompressible material response, see, e.g. [7]. For a complete review and bibliography of works on numerical modeling of rubber-like materials, we refer the reader to [8, 9]. Many finite element (FE) formulations have been developed to avoid the volumetric locking resulting from the incompressibility constraint. Among them are the mixed formulation [10–12], the hybrid methods [13–15], the selective reduced integration [16], the perturbed Lagrange formulation [17], and the rank-one filtering method [18]. In addition to difficulties in dealing with incompressibility, FE formulations frequently break down when applied to elastomers where excessive deformations lead to mesh entanglement.

Recently, considerable research in computational mechanics has been devoted to the development of meshless methods. These methods alleviate the difficulty of meshing and remeshing the entire structure, by only adding or deleting nodes at suitable locations. Meshless methods may also alleviate some other problems associated with the FE method, such as element distortion. During the last two decades, several meshless methods for seeking approximate solutions of partial differential equations have been proposed; these include the element-free Galerkin (EFG) [19], hp-clouds [20], the reproducing kernel particle [21], the smoothed particle hydrodynamics (SPH) [22], the diffuse element [23], the partition of unity FE [24], the natural element [25], meshless Galerkin using radial basis functions [26], the meshless local Petrov–Galerkin (MLPG) [27], the modified smoothed particle hydrodynamics (MSPH) [28], and the collocation method with radial basis functions [29]. All of these methods, except for the MLPG, the SPH, the MSPH, and the collocation are not truly meshless since the use of shadow elements is required for evaluating integrals appearing in the governing weak formulations [30]. The MLPG method has been successfully applied to several structural problems: static linear plane elasticity [27]; vibrations of elastic planar bodies [31]; static analysis of thin plates [32]; static analysis of beams [33]; vibrations of cracked beams [33]; static and dynamic problems for functionally graded materials [34, 35]; analysis of transient problems with material discontinuities [36]; analysis of microelectromechanical problems [37, 38]; high-speed impact penetration mechanics [39]; and analysis of large deformation problems [40].

The MLPG method is based on local weak form of governing equations and employs meshless interpolations for both the trial and test functions. The trial functions are constructed by using the moving-least squares (MLS) [41] approximation which relies on the location of points or nodes in

DOI: 10.1002/cnm

the body. In the Petrov–Galerkin formulation, test functions may be chosen from a different space than the space of trial functions, resulting in several variations of the method, see e.g. [30]. Thus, the key ingredients of the MLPG method may be summarized as local weak formulation, MLS interpolation, and Petrov–Galerkin projection. Key issues to be addressed in formulating an MLPG method are the evaluation of domain integrals appearing in the weak formulation, imposition of essential boundary conditions, and for transient problems time integration of the resulting ordinary differential equations.

Here we analyze finite static deformations of rubber-like materials with the MLPG method. We derive a local mixed weak formulation in which both the pressure and displacement fields are regarded as unknowns. By splitting the strain energy density into deviatoric and dilatational parts, we treat simultaneously problems for nearly incompressible and fully incompressible materials. The essential boundary conditions are imposed through a set of Lagrange multipliers defined on the boundary. We adopt the concept of secondary nodes developed in [42] for enriching the set of trial functions without increasing noticeably the computational cost. The method is applied to the solution of different plane strain sample problems, and it is shown that their accurate solution can be computed with very few nodes. Moreover, it is shown that when a purely displacement formulation is adopted in the MLPG method, a locking phenomenon similar to that encountered in the FE method occurs, suggesting thereby the need for a mixed formulation.

The main contributions of the paper are the derivation of a mixed local weak formulation of the non-linear problem where the displacement, pressure and constraint reactions are treated as unknowns that is applicable to completely incompressible or nearly incompressible materials; showing that pure displacement meshless formulations do not avoid locking phenomenon; adapting the secondary nodes to non-linear problems, and demonstrating that accurate approximate solutions can be obtained with a few nodes.

The rest of the paper is organized as follows. In Section 2 we derive a local symmetric weak formulation valid for hyperelastic materials and then we specialize it to the analysis of plane strain deformations of rubber-like materials. Section 2 presents the MLPG discrete non-linear equations for determining an approximate solution. In Section 3, we apply the proposed method to the solution of linear and non-linear problems. Section 4 addresses solutions of plane stress problems. Section 5 summarizes conclusions of this work. The Appendix describes the MLS approximation for generating basis functions to approximate the trial solution using secondary nodes, and the elasticity tensor for a nearly incompressible hyperelastic isotropic material.

2. APPLICATION OF THE MLPG METHOD TO NON-LINEAR ELASTIC PROBLEMS

2.1. Local weak formulation

Following [43], we consider three distinct configurations of a body in the Euclidean space: the reference configuration Ω, an intermediate one Ω^0, and the present one Ω^t. Material points in Ω are indicated by $\mathbf{x}$, those in Ω^0 by $\mathbf{x}^0$, and those in Ω^t by $\mathbf{x}^t$. A field (scalar or tensor) $\mathbf{q}$ in the reference configuration is indicated by $\mathbf{q}^0$ or $\mathbf{q}^t$ when pushed forward in the intermediate or in the actual configuration, respectively; while its increment from the intermediate to the actual configuration is denoted by $\Delta\mathbf{q}(\mathbf{x})$. Furthermore, $\mathbf{w}$ indicates the displacement vector, $\mathbf{F}$ the deformation gradient, $\mathbf{C}$ the right Cauchy–Green strain tensor, $\mathbf{E}$ the Green–St.Venant strain tensor, $\mathbf{S}$ the second Piola–Kirchhoff stress tensor, and $\mathbf{P}$ the first Piola–Kirchhoff stress tensor.

DOI: 10.1002/cnm

A mixed pressure/displacement formulation is used here; the stress tensor depends on both the Green–St.Venant strain tensor $\mathbf{E}$ and the pressure field p. The boundary $\partial\Omega$ of the domain Ω is partitioned into two disjoint parts:

$$\partial\Omega = \Gamma_{\mathbf{w}} \cup \Gamma_{\mathbf{t}}$$

On the boundary $\Gamma_{\mathbf{w}}$ displacements are prescribed as

$$\mathbf{w}^t(\mathbf{x}) = \bar{\mathbf{w}}(\mathbf{x}), \quad \mathbf{x} \in \Gamma_{\mathbf{w}}$$

while on the boundary $\Gamma_{\mathbf{t}}$ dead loads are prescribed by

$$\mathbf{P}^t(\mathbf{x})\mathbf{n}(\mathbf{x}) = \bar{\mathbf{t}}(\mathbf{x}), \quad \mathbf{x} \in \Gamma_{\mathbf{t}}$$

where $\mathbf{n}$ is the outward unit normal to $\Gamma_{\mathbf{t}}$.

For a generic subdomain Ω_s of domain Ω, the principle of virtual work (see e.g. [44]) gives

$$\int_{\Omega_s} \mathbf{S}^t(\mathbf{x}) \cdot \mathrm{Sym}[(\mathbf{F}^t)^{\mathrm{T}}(\mathbf{x}) \nabla \boldsymbol{\varphi}(\mathbf{x})] \, \mathrm{d}\Omega = \int_{\Omega_s} \mathbf{b}(\mathbf{x}) \cdot \boldsymbol{\varphi}(\mathbf{x}) \, \mathrm{d}\Omega + \int_{\partial\Omega_s} \mathbf{P}^t(\mathbf{x})\mathbf{n}(\mathbf{x}) \cdot \boldsymbol{\varphi}(\mathbf{x}) \, \mathrm{d}\Gamma$$

where $\boldsymbol{\varphi}$ is a virtual displacement or a test function that does not need to vanish on $\Gamma_{\mathbf{w}}$, ∇ is the gradient with respect to reference coordinates, Sym indicates the symmetric part, and superscript T indicates transposition.

The boundary $\partial\Omega_s$ can be divided into three disjoint parts $\partial\Omega_s = L_s \cup \Gamma_{\mathbf{ts}} \cup \Gamma_{\mathbf{ws}}$. The curve L_s lies inside the domain Ω, $\Gamma_{\mathbf{ts}}$ equals the part of $\partial\Omega_s$ where natural boundary conditions are prescribed, and $\Gamma_{\mathbf{ws}}$ specifies the part of $\partial\Omega_s$ where essential boundary conditions are prescribed. Hence, by substituting for the traction boundary condition we obtain

$$\int_{\partial\Omega_s} \mathbf{P}^t(\mathbf{x})\mathbf{n}(\mathbf{x}) \cdot \boldsymbol{\varphi}(\mathbf{x}) \, \mathrm{d}\Gamma = \int_{L_s} \mathbf{P}^t(\mathbf{x})\mathbf{n}(\mathbf{x}) \cdot \boldsymbol{\varphi}(\mathbf{x}) \, \mathrm{d}\Gamma + \int_{\Gamma_{\mathbf{ts}}} \bar{\mathbf{t}}(\mathbf{x}) \cdot \boldsymbol{\varphi}(\mathbf{x}) \, \mathrm{d}\Gamma + \int_{\Gamma_{\mathbf{ws}}} \mathbf{r}^t(\mathbf{x}) \cdot \boldsymbol{\varphi}(\mathbf{x}) \, \mathrm{d}\Gamma$$

where

$$\mathbf{r}^t(\mathbf{x}) = \mathbf{P}^t(\mathbf{x})\mathbf{n}(\mathbf{x})$$

represents the unknown constraint reaction field in the reference configuration acting at boundary points with prescribed displacements. By choosing test functions that vanish on the interior contour L_s, the weak formulation of the non-linear problem in the reference configuration is

$$\int_{\Omega_s} \mathbf{S}^t(\mathbf{x}) \cdot \mathrm{Sym}[(\mathbf{F}^t)^{\mathrm{T}}(\mathbf{x}) \nabla \boldsymbol{\varphi}(\mathbf{x})] \, \mathrm{d}\Omega = \int_{\Omega_s} \mathbf{b}(\mathbf{x}) \cdot \boldsymbol{\varphi}(\mathbf{x}) \, \mathrm{d}\Omega + \int_{\Gamma_{\mathbf{ts}}} \bar{\mathbf{t}}(\mathbf{x}) \cdot \boldsymbol{\varphi}(\mathbf{x}) \, \mathrm{d}\Gamma + \int_{\Gamma_{\mathbf{ws}}} \mathbf{r}^t(\mathbf{x}) \cdot \boldsymbol{\varphi}(\mathbf{x}) \, \mathrm{d}\Gamma \tag{1}$$

In order to impose essential boundary conditions on $\Gamma_{\mathbf{w}}$ in a weak local sense, we consider the additional integral equation

$$\int_{\gamma_s} \mathbf{w}^t(\mathbf{x}) \cdot \boldsymbol{\lambda}(\mathbf{x}) \, \mathrm{d}\Gamma = \int_{\gamma_s} \bar{\mathbf{w}}(\mathbf{x}) \cdot \boldsymbol{\lambda}(\mathbf{x}) \, \mathrm{d}\Gamma \tag{2}$$

DOI: 10.1002/cnm

where $\boldsymbol{\lambda}$ is a smooth test field defined on the portion γ_s of $\Gamma_{\mathbf{w}}$. We note that γ_s plays the same role for the boundary $\Gamma_{\mathbf{w}}$ as Ω_s does for Ω.

The full or nearly incompressibility condition is accommodated by requiring that

$$p^t(\mathbf{x}) = \bar{p}^t(\mathbf{E}^t(\mathbf{x})) \tag{3}$$

where $\bar{p}^t$ is the pressure computed from the deformation gradient. This leads to the local weak formulation

$$\int_{\Omega_s} p^t(\mathbf{x})\xi(\mathbf{x})\,\mathrm{d}\Omega = \int_{\Omega_s} \bar{p}^t(\mathbf{x})\xi(\mathbf{x})\,\mathrm{d}\Omega \tag{4}$$

where ξ is a smooth test field defined on Ω_s.

2.2. *Total Lagrangian mixed formulation*

In order to derive a total Lagrangian formulation (see e.g. [43]) of the problem suitable for numerical implementation, we regard the present configuration as differing by an infinitesimal amount from the intermediate configuration and linearize the weak formulation around the intermediate configuration.

Therefore, we adopt the following incremental form of the stress tensor:

$$\mathbf{S}^t(\mathbf{x}) \simeq \mathbf{S}^0(\mathbf{x}) + \mathbb{C}(\mathbf{x})(\mathbf{E}^t(\mathbf{x}) - \mathbf{E}^0(\mathbf{x})) + \mathbf{H}(\mathbf{x})(p^t(\mathbf{x}) - p^0(\mathbf{x})) \tag{5}$$

where

$$\mathbb{C} = \left.\frac{\partial \mathbf{S}}{\partial \mathbf{E}}\right|_0, \qquad \mathbf{H} = \left.\frac{\partial \mathbf{S}}{\partial p}\right|_0$$

and $\cdot|_0$ implies that the quantity is evaluated in the intermediate configuration. The constitutive relation (5) is still non-linear in the displacement increment $\Delta\mathbf{w}$ from Ω^0 to Ω^t, since the difference of the two strains is not linear in the gradient of the incremental displacement. However, since

$$\mathbf{E}^t - \mathbf{E}^0 \simeq \mathrm{Sym}[(\mathbf{F}^0)^{\mathrm{T}}\nabla\Delta\mathbf{w}], \quad \Delta\mathbf{w} = \mathbf{w}^t - \mathbf{w}^0$$

we obtain the following linearized constitutive equation:

$$\mathbf{S}^t \simeq \mathbf{S}^0 + \mathbb{C}\mathrm{Sym}[(\mathbf{F}^0)^{\mathrm{T}}\nabla\Delta\mathbf{w}] + \mathbf{H}\Delta p \tag{6}$$

Substituting for $\mathbf{S}^t$ from (6) into (1), and decomposing the virtual work done by the external forces in the right-hand side of (1) into the virtual work done by loads that keep the body in equilibrium in the intermediate configuration, and the virtual work done by the incremental loads, the incremental form of the symmetric weak formulation (1) becomes

$$\int_{\Omega_s} \nabla\Delta w\mathbf{S}^0 \cdot \nabla\boldsymbol{\varphi}\,\mathrm{d}\Omega + \int_{\Omega_s} \mathbb{C}\mathrm{Sym}[(\mathbf{F}^0)^{\mathrm{T}}\nabla\Delta\mathbf{w}] \cdot \mathrm{Sym}[(\mathbf{F}^0)^{\mathrm{T}}\nabla\boldsymbol{\varphi}]\,\mathrm{d}\Omega$$
$$+ \int_{\Omega_s} \Delta p\mathbf{H} \cdot \mathrm{Sym}[(\mathbf{F}^0)^{\mathrm{T}}\nabla\boldsymbol{\varphi}] - \int_{\Gamma_{ws}} \Delta\mathbf{r}(\mathbf{x}) \cdot \boldsymbol{\varphi}(\mathbf{x})\,\mathrm{d}\Gamma$$

DOI: 10.1002/cnm

$$= \int_{\Omega_s} \mathbf{b}^0(\mathbf{x}) \cdot \boldsymbol{\varphi}(\mathbf{x})\, d\Omega + \int_{\Gamma_{ts}} \bar{\mathbf{t}}^0(\mathbf{x}) \cdot \boldsymbol{\varphi}(\mathbf{x})\, d\Gamma + \int_{\Gamma_{ws}} \mathbf{r}^0(\mathbf{x}) \cdot \boldsymbol{\varphi}(\mathbf{x})\, d\Gamma$$
$$- \int_{\Omega_s} \mathbf{S}^0 \cdot \mathrm{Sym}[(\mathbf{F}^0)^{\mathrm{T}} \nabla \boldsymbol{\varphi}]\, d\Omega + \int_{\Omega_s} \Delta\mathbf{b}(\mathbf{x}) \cdot \boldsymbol{\varphi}(\mathbf{x})\, d\Omega + \int_{\Gamma_{ts}} \Delta\bar{\mathbf{t}}(\mathbf{x}) \cdot \boldsymbol{\varphi}(\mathbf{x})\, d\Gamma \tag{7}$$

In order to determine the incremental displacement field, the incremental pressure field, and the constraint reactions, we consider also the incremental forms of Equations (2) and (4), i.e.

$$\int_{\gamma_s} \Delta\mathbf{w}(\mathbf{x}) \cdot \boldsymbol{\lambda}(\mathbf{x})\, d\Gamma = \int_{\gamma_s} \Delta\bar{\mathbf{w}}(\mathbf{x}) \cdot \boldsymbol{\lambda}(\mathbf{x})\, d\Gamma \tag{8}$$

and

$$\int_{\Omega_s} \Delta p(\mathbf{x}) \xi(\mathbf{x})\, d\Omega - \int_{\Omega_s} (\mathbf{Q} \cdot \mathrm{Sym}[(\mathbf{F}^0)^{\mathrm{T}} \nabla \Delta\mathbf{w}]) \xi(\mathbf{x})\, d\Omega$$
$$= - \int_{\Omega_s} p^0(\mathbf{x}) \xi(\mathbf{x})\, d\Omega + \int_{\Omega_s} \bar{p}^0(\mathbf{x}) \xi(\mathbf{x})\, d\Omega \tag{9}$$

where

$$\mathbf{Q} = \left. \frac{\partial \bar{p}}{\partial \mathbf{E}} \right|_0$$

Henceforth, we consider only plane strain problems with deformations in the x_1x_2, where x_1 and x_2 define a Cartesian coordinate system, and set

$$\Delta\mathbf{d} = \begin{Bmatrix} \dfrac{\partial \Delta w_1}{\partial x_1} \\ \dfrac{\partial \Delta w_1}{\partial x_2} \\ \dfrac{\partial \Delta w_2}{\partial x_1} \\ \dfrac{\partial \Delta w_2}{\partial x_2} \end{Bmatrix}, \quad \Delta\mathbf{w} = \begin{Bmatrix} \Delta w_1 \\ \Delta w_2 \end{Bmatrix}, \quad \Delta\mathbf{r} = \begin{Bmatrix} \Delta r_1 \\ \Delta r_2 \end{Bmatrix}, \quad \Delta\mathbf{b} = \begin{Bmatrix} \Delta b_1 \\ \Delta b_2 \end{Bmatrix}, \quad \Delta\bar{\mathbf{t}} = \begin{Bmatrix} \Delta \bar{t}_1 \\ \Delta \bar{t}_2 \end{Bmatrix}$$

$$\boldsymbol{\delta} = \begin{Bmatrix} \dfrac{\partial \varphi_1}{\partial x_1} \\ \dfrac{\partial \varphi_1}{\partial x_2} \\ \dfrac{\partial \varphi_2}{\partial x_1} \\ \dfrac{\partial \varphi_2}{\partial x_2} \end{Bmatrix}, \quad \boldsymbol{\varphi} = \begin{Bmatrix} \varphi_1 \\ \varphi_2 \end{Bmatrix}, \quad \Delta\boldsymbol{\lambda} = \begin{Bmatrix} \Delta\lambda_1 \\ \Delta\lambda_2 \end{Bmatrix}, \quad \mathbf{w}^0 = \begin{Bmatrix} w_1^0 \\ w_2^0 \end{Bmatrix}, \quad \mathbf{r}^0 = \begin{Bmatrix} r_1^0 \\ r_2^0 \end{Bmatrix}$$

DOI: 10.1002/cnm

$$\mathbf{S}^0=\begin{bmatrix} S_{11}^0 & S_{12}^0 & 0 & 0 \\ S_{12}^0 & S_{22}^0 & 0 & 0 \\ 0 & 0 & S_{11}^0 & S_{12}^0 \\ 0 & 0 & S_{12}^0 & S_{22}^0 \end{bmatrix}, \quad \mathbf{B}=\begin{bmatrix} 1+\dfrac{\partial w_1^0}{\partial x_1} & 0 & \dfrac{\partial w_2^0}{\partial x_1} & 0 \\ 0 & \dfrac{\partial w_1^0}{\partial x_2} & 0 & 1+\dfrac{\partial w_2^0}{\partial x_2} \\ \dfrac{\partial w_1^0}{\partial x_2} & 1+\dfrac{\partial w_1^0}{\partial x_1} & 1+\dfrac{\partial w_2^0}{\partial x_2} & \dfrac{\partial w_2^0}{\partial x_1} \end{bmatrix}$$

$$\mathbf{Q}=\begin{Bmatrix} Q_{11} \\ Q_{22} \\ Q_{12} \end{Bmatrix}, \quad \mathbf{H}=\begin{Bmatrix} H_{11} \\ H_{22} \\ H_{12} \end{Bmatrix}, \quad \mathbf{s}^0=\begin{Bmatrix} S_{11}^0 \\ S_{22}^0 \\ S_{12}^0 \end{Bmatrix}, \quad \mathbf{b}^0=\begin{Bmatrix} b_1^0 \\ b_2^0 \end{Bmatrix}, \quad \bar{\mathbf{t}}^0=\begin{Bmatrix} \bar{t}_1^0 \\ \bar{t}_2^0 \end{Bmatrix}$$

In this notation Equations (7), (8) and (9) can be expressed as

$$\begin{aligned} &\int_{\Omega_s} \boldsymbol{\delta}^{\mathrm{T}}(\mathbb{B}+\mathbf{S}^0)\Delta\mathbf{d}\,\mathrm{d}\Omega+\int_{\Omega_s}\boldsymbol{\delta}^{\mathrm{T}}\mathbb{H}\Delta p\,\mathrm{d}\Omega-\int_{\Gamma_{ws}}\boldsymbol{\varphi}^{\mathrm{T}}\Delta\mathbf{r}\,\mathrm{d}\Gamma \\ &\quad=-\int_{\Omega_s}\boldsymbol{\delta}^{\mathrm{T}}\mathbb{S}\,\mathrm{d}\Omega+\int_{\Omega_s}\boldsymbol{\varphi}^{\mathrm{T}}\mathbf{b}^0\,\mathrm{d}\Omega+\int_{\Gamma_{ts}}\boldsymbol{\varphi}^{\mathrm{T}}\bar{\mathbf{t}}^0\,\mathrm{d}\Gamma+\int_{\Gamma_{ws}}\boldsymbol{\varphi}^{\mathrm{T}}\mathbf{r}^0\,\mathrm{d}\Gamma \\ &\qquad+\int_{\Omega_s}\boldsymbol{\varphi}^{\mathrm{T}}\Delta\mathbf{b}\,\mathrm{d}\Omega+\int_{\Gamma_{ts}}\boldsymbol{\varphi}^{\mathrm{T}}\Delta\bar{\mathbf{t}}\,\mathrm{d}\Gamma \end{aligned} \tag{10}$$

$$\int_{\gamma_s}\boldsymbol{\lambda}^{\mathrm{T}}\Delta\mathbf{w}\,\mathrm{d}\Gamma=\int_{\gamma_s}\boldsymbol{\lambda}^{\mathrm{T}}\Delta\bar{\mathbf{w}}\,\mathrm{d}\Gamma \tag{11}$$

$$\int_{\Omega_s}\xi\Delta p\,d\Omega-\int_{\Omega_s}\xi\mathbb{Q}^{\mathrm{T}}\Delta\mathbf{d}\,\mathrm{d}\Omega=\int_{\Omega_s}\xi(\bar{p}^0-p^0)\,\mathrm{d}\Omega \tag{12}$$

where

$$\mathbb{B}=\mathbf{B}^{\mathrm{T}}\mathbf{L}\mathbf{B}, \quad \mathbb{S}=\mathbf{B}^{\mathrm{T}}\mathbf{s}^0, \quad \mathbb{H}=\mathbf{B}^{\mathrm{T}}\mathbf{H}, \qquad \mathbb{Q}=\mathbf{B}^{\mathrm{T}}\mathbf{Q}$$

and $\mathbf{L}$ is the elasticity matrix. We note that matrices $\mathbf{S}^0$, $\mathbf{B}$, $\mathbf{L}$, $\mathbf{H}$, and $\mathbf{Q}$ depend on the state of deformation and on pressure in the intermediate configuration.

The preceding formulation differs from that used earlier, e.g. [11], in the following respects. Here, constraint reactions are determined as a part of the solution of the problem, and the pressure field is given by (3). In [11], the pressure is regarded as a Lagrange multiplier to impose the incompressibility constraint. Whereas in EFG, e.g. [19], the region Ω_s in Equations (10)–(12) equals the entire region Ω occupied by the body in the reference configuration, here $\Omega_s \subset \Omega$ is a subregion of Ω. Furthermore, as should become clear from the following material, there is no background mesh used to numerically integrate Equations (10)–(12).

DOI: 10.1002/cnm

2.3. Discrete formulation

In order to find an approximate solution of the linearized elastic problem, we approximate components of the displacement and the pressure fields by using N 2-D MLS basis functions given by Equation (A8) in the Appendix:

$$w_1(\mathbf{x}) = \boldsymbol{\psi}^{\mathrm{T}}(\mathbf{x})\hat{\mathbf{w}}_1, \quad w_2(\mathbf{x}) = \boldsymbol{\psi}^{\mathrm{T}}(\mathbf{x})\hat{\mathbf{w}}_2, \quad p(\mathbf{x}) = \boldsymbol{\psi}^{\mathrm{T}}(\mathbf{x})\hat{\mathbf{p}}$$

The constraint reactions field is instead approximated by using $2N_B$ 1-D MLS basis functions obtained from (A8) by discretizing the boundary of the domain by piecewise linear segments, and by placing a set of nodes on each segment, i.e.

$$r_1(\mathbf{x}) = \boldsymbol{\chi}(\mathbf{x})^{\mathrm{T}}\hat{\mathbf{r}}_1, \quad r_2(\mathbf{x}) = \boldsymbol{\chi}(\mathbf{x})^{\mathrm{T}}\hat{\mathbf{r}}_2$$

For convenience we group nodal displacements and nodal reactions into two vectors $\hat{\mathbf{w}}$ to $\hat{\boldsymbol{\lambda}}$. In order to obtain a set of linearly independent algebraic equations for the $3N+2N_B$ nodal unknowns, we use N local 2-D subdomains Ω_{si}, N_B local 1-D subdomains γ_{si}, N independent scalar test fields φ_i defined on each Ω_{si} and vanishing on L_{si}, and N_B independent scalar test fields ϕ_i defined on γ_{si}. Note that subdomains Ω_{si} and γ_{si} do not need to be disjoint. We thus get the following algebraic problem:

$$\begin{bmatrix} \mathbf{K_{ww}} & \mathbf{K_{wp}} & \mathbf{K_{wr}} \\ \mathbf{K_{pw}} & \mathbf{K_{pp}} & \mathbf{0} \\ \mathbf{K_{rw}} & \mathbf{0} & \mathbf{0} \end{bmatrix} \begin{Bmatrix} \hat{\mathbf{w}} \\ \hat{\mathbf{p}} \\ \hat{\mathbf{r}} \end{Bmatrix} = \begin{Bmatrix} \Delta\mathbf{f}_w \\ \mathbf{0} \\ \Delta\mathbf{f}_r \end{Bmatrix} + \begin{Bmatrix} \mathbf{f}_w \\ \mathbf{0} \\ \mathbf{f}_r \end{Bmatrix} + \begin{Bmatrix} \mathbf{R}_w \\ \mathbf{R}_p \\ \mathbf{R}_r \end{Bmatrix} \tag{13}$$

where the explicit form of the tangent stiffness matrix and of the load vector can be deduced from Equations (10)–(12). For problems involving dead loads, as those studied in this paper, the incremental load is a given constant vector, and the tangent stiffness matrix and the residual loads depend on the deformation and pressure fields in the intermediate configuration.

An alternative to the MLS basis functions is the SSPH basis functions [45] wherein the function and its derivatives of the desired degree at a point are expressed in terms of the values of the function at discrete points.

3. COMPUTATION AND DISCUSSION OF RESULTS

In order to validate the problem formulation and the developed computer code, we consider a square plate of side 1, and we numerically analyze several problems and compare our findings to either exact or FE solutions.

We take test functions from the same space as the trial solutions. We consider a regular grid of 49 primary nodes as shown in Figure 1. Linear monomial basis, $m=3$, is used to generate the MLS basis functions, and the origin of the coordinate axes is located at the bottom left corner. Weight functions with square supports are used, and the size r_i of their support is chosen to be $\frac{1}{2}$. This guarantees the non-singularity of matrices in the MLS approximation, since r_i equals three times the nodal spacing. For the considered problems, we found through numerical experiments that this supports' size represents a good compromise between computational speed and accuracy. Larger supports generally result in more accurate solutions but require more computational effort, see, e.g. [46]. Values assigned to other constants defining weight functions in Equation (A9) are

DOI: 10.1002/cnm

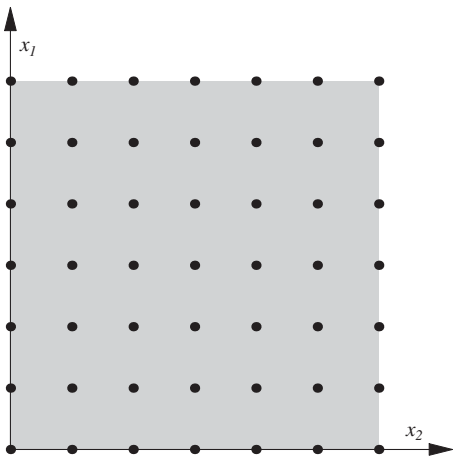

Figure 1. Geometry and locations of primary nodes for the sample problem studied.

$k=1$, $c_i=r_i/4$. To numerically evaluate integrals appearing in the linearized weak formulation of the problem, we use 6×6 quadrature points in each intersection of supports of weight functions associated with different primary nodes. This approach extends to two-dimensional problems the technique developed in [33] to increase the accuracy of numerical integration. The approach noticeably differs from the background mesh concept of the EFG methods [19], since integration domains are not *a priori* assigned in a mesh-like manner but are dynamically constructed based on the nodes' locations. We note that, for the considered nodes' distribution, the smallest intersection among the weight functions' supports is a square of side $\frac{1}{6}$. This leads to a considerably limited number of quadrature points.

We first solve a linear elastic problem for a homogeneous and isotropic cantilever plate to show advantages of the mixed formulation with respect to the pure displacement formulation. We show that as Poisson's ratio v approaches $\frac{1}{2}$ the pure displacement formulation locks. In this case, the numerical solution is obtained by solving (13) with zero initial stresses, and

$$\mathbb{B}=\frac{E}{2(1+v)}\begin{bmatrix} 4/3 & 0 & 0 & -2/3 \\ 0 & 1 & 1 & 0 \\ 0 & 1 & 1 & 0 \\ -2/3 & 0 & 0 & 4/3 \end{bmatrix}, \quad \mathbb{H}=\begin{Bmatrix} 1 \\ 0 \\ 0 \\ 1 \end{Bmatrix}, \quad \mathbb{Q}=-\frac{E}{2(1+v)(1-2v)}\mathbb{P} \tag{14}$$

E being Young's modulus. For this linear problem, exact and MLPG results are compared in terms of tip deflection.

Problems 2, 3, 4, and 5 focus on finite deformations of Mooney–Rivlin materials under different loadings and boundary conditions; they represent, respectively, the uniform extension, non-uniform extension, uniform shear, and non-uniform shear. These problems are solved using the method of fictitious loads, see, for example, remarks after Equation (30) of [47]. In particular, we choose an isochoric deformation and determine the corresponding body forces and surface tractions from the Mooney–Rivlin constitutive relation given in Appendix and the balance laws. The pressure field corresponding to an isochoric deformation, see Equation (3), is zero since the bulk modulus k

DOI: 10.1002/cnm

is finite. The following L^2 logarithmic error norm is used to compare computed results with the exact solution:

$$\text{ERR} = \log_{10} \frac{\sqrt{\int_\Omega [(w_1^{\text{EX}} - w_1^{\text{MLPG}})^2 + (w_2^{\text{EX}} - w_2^{\text{MLPG}})^2]\, d\Omega}}{\sqrt{\int_\Omega [(w_1^{\text{EX}})^2 + (w_2^{\text{EX}})^2]\, d\Omega}} \tag{15}$$

where superscripts EX and MLPG stand for the exact and the numerical solutions, respectively. Stress distributions are fairly smooth and numerical findings are in very good agreement with exact solutions. Quantitative results are only shown for displacements.

Problem 6 analyzes the stress intensity factor in a body made of a Mooney–Rivlin material undergoing either small or large mode-I deformations. In this case, we use secondary nodes presented in the Appendix to improve the solution accuracy. The size of the support of the weight function of a secondary node in Equation (A10) equals the maximum distance between a secondary node and its associated primary node. We compare the numerical value of the J-integral to the exact one for small deformations. For large deformations, analytical solutions do not exist; we compare the MLPG solution with a FE solution and show the behavior of the stress field close to the crack tip.

For all finite deformation problems, parameters for the Mooney–Rivlin material, defined in the Appendix, are

$$A_{10} = 1, \quad A_{20} = 0.05, \quad k = 10^3$$

The non-linear problems are solved by the Newton–Raphson method [5] with the total load divided into small increments, and the load increment changed according to the number of iterations needed for the solution to converge. The norm of the incremental solution in Newton's iterations is computed by using the norm of the interpolated fields rather than that of the fictitious nodal values.

3.1. Linear elastic problem for a cantilever

We consider the cantilever beam problem studied in [48] for which the exact solution is

$$w_1 = -\frac{2P}{Eb^3}\left(x_2 - \frac{b}{2}\right)\left[3x_1(2b - x_1) + \left(2 + \frac{v}{1-v}\right)x_2(x_2 - b)\right]$$

$$w_2 = \frac{2P}{Eb^3}\left[(x_1)^2(3b - x_1) + 3\frac{v}{1-v}(b - x_1)\left(x_2 - \frac{b}{2}\right)^2 + \left(4 + \frac{5v}{1-v}\right)b^2 x_1\right]$$

where the right edge is clamped, a distributed load with resultant P is applied on the left edge, b is the height of the beam, and its width is one. In a consistent set of units the problem is analyzed for $P = -0.1$, $E = 1$, and $v = 0.4, 0.499$ and 0.49999999. In Table I we report results of the mixed and the pure displacement formulations in terms of the tip deflection for the three values of v. The pure displacement formulation essentially locks when the incompressibility constraint is severe, while the mixed formulation is insensitive to variations of Poisson's ratio in the neighborhood of $\frac{1}{2}$. Thus, the pure displacement formulation may not give accurate results as $v \to \frac{1}{2}$.

Locking of the pure displacement formulation is also shown in Problem 6 when exact and numerically evaluated values of J-integrals for a cracked plate are compared.

DOI: 10.1002/cnm

Table I. For a cantilever beam, percentage error in the tip deflection computed with mixed and pure displacement MLPG formulations.

	Pure displacement	Mixed
$v=0.4$	0.60	1.20
$v=0.499$	6.59	0.79
$v=0.49999999$	10.9	0.80

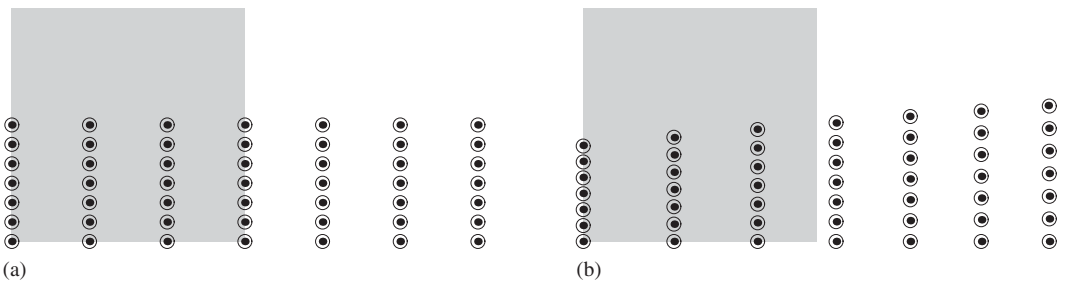

Figure 2. (a) Uniform extension of a plate and (b) non-uniform extension of a plate. Undeformed configuration (shaded), exact solution (empty circles), MLPG solution (dots).

3.2. Uniform extension

We consider simple tensile deformations of a plate and assume that its left and bottom edges are on rollers, while tractions act on the other two edges as determined by substituting the following isochoric deformation field in the Mooney–Rivlin constitutive relation:

$$f_1(x_1, x_2) = 2x_2, \quad f_2(x_1, x_2) = \tfrac{1}{2}x_1$$

The logarithmic norm (15) of the error in displacements is -4.51. In Figure 2(a) we show the initial shape of the plate, the final locations of nodes resulting from the exact solution (empty circle), and the MLPG solution (dots). For this problem no body forces are present and the high accuracy of the computed solution depends strongly on the linearity of the displacement field that can be reproduced exactly by the MLS basis functions.

3.3. Non-uniform extension

We now analyze inhomogeneous finite deformations of the plate. We assume that the plate is supported on rollers on the left and bottom edges, and body forces and surface tractions are applied according to the stress field determined by the Mooney–Rivlin constitutive relation with the isochoric deformation field:

$$f_1(x_1, x_2) = x_1 + \log(x_1+1)\frac{1}{\log 2}$$

$$f_2(x_1, x_2) = x_2\frac{(x_1+1)\log 2}{(x_1+1)\log 2+1} + \log(x_1+1)\frac{1}{\log 2}$$

DOI: 10.1002/cnm

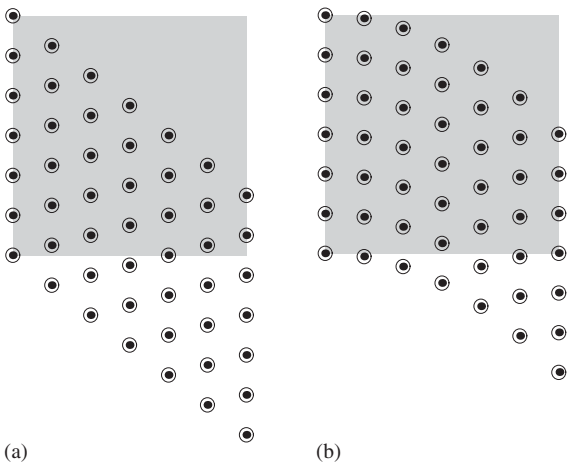

Figure 3. (a) Uniform shear of a plate, and (b) non-uniform shear of a plate. Undeformed configuration (shaded), exact solution (empty circles), MLPG solution (dots).

The logarithmic norm (15) of the error in computed displacements is -2.78. In Figure 2(b) we observe the initial shape of the plate and the final locations of the nodes resulting from the exact solution (empty circle) and the MLPG solution (dots).

3.4. Uniform shear

We study uniform shear deformations by clamping the left edge of the square plate, and by loading other edges as determined by substituting the following isochoric deformation field into the Mooney–Rivlin constitutive relation:

$$f_1(x_1, x_2) = x_1, \quad f_2(x_1, x_2) = x_2 - \tfrac{3}{4}x_1$$

The logarithmic norm (15) of the error in displacements is -3.84. In Figure 3(a) we exhibit the initial shape of the plate, and the final locations of nodes resulting from the exact solution (empty circle) and the MLPG solution (dots). For this case the same comments as those for the homogeneous extension apply.

3.5. Non-uniform shear

We assume that the plate is clamped at the left edge, and body forces and surface tractions are applied according to the stress field determined by the Mooney–Rivlin constitutive relation with the deformation field:

$$f_1(x_1, x_2) = x_1, \quad f_2(x_1, x_2) = x_2 - \tfrac{1}{2}(x_1)^2$$

The logarithmic norm (15) of the error in displacements computed by the MLPG method is -2.48. In Figure 3(b) we evince the initial shape of the plate and the final locations of nodes resulting from the exact solution (empty circle) and the MLPG solution (dots).

DOI: 10.1002/cnm

3.6. Crack problem

We consider a cracked plate whose geometry is exhibited in Figure 4(a). By exploiting the symmetry of the problem, we numerically analyze deformations of the quarter of the domain depicted in Figure 4(b). In order to accurately analyze effects of the crack, we use secondary nodes in the neighborhood of the crack tip, all over the domain, and on the boundaries as shown in Figure 5(a). The secondary nodes located in the neighborhood of the crack tip are needed for accurately estimating the stress concentration there. The secondary nodes on the boundaries and in the domain are needed for satisfying well the boundary conditions and improving the solution inside the domain. From numerical experiments we have observed that locating only secondary nodes in the neighborhood of the crack tip leads to poor solutions with spurious pressure modes. The total number of nodes used in the simulation is 168.

The plate is loaded with a uniformly distributed dead load $\sigma_0 = 0.65$, and the crack length equals one-half of the plate width. In Figure 5(b) we exhibit the deformed shape of the quarter of the plate. Recalling that nominal tractions are prescribed on the top surface of the plate, it does not need to stay horizontal during the deformation process. Also, the total axial force stays constant even though the width of the plate decreases.

The J-integral in finite elasticity is given by (see, e.g. [49])

$$J = \int_{\Gamma} \left(W n_1 - \mathbf{n} \cdot \mathbf{P}^t \frac{\partial \mathbf{w}^t}{\partial x_1} \right) \mathrm{d}\Gamma$$

where Γ is the integration contour surrounding the crack tip in the reference configuration, W is the strain energy density (e.g. see Equation (B2)), $\mathbf{n}$ is the unit outward normal to Γ, and n_1 is its component in the crack direction. In order to evaluate J, we use a circular contour of radius 0.125 centered at the crack tip.

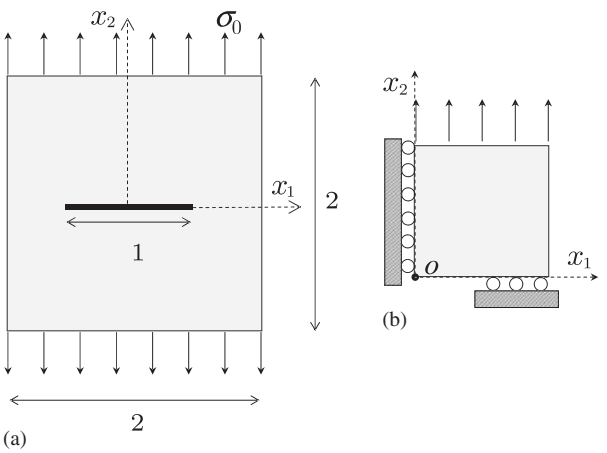

Figure 4. Geometry of a cracked plate loaded in mode-I.

DOI: 10.1002/cnm

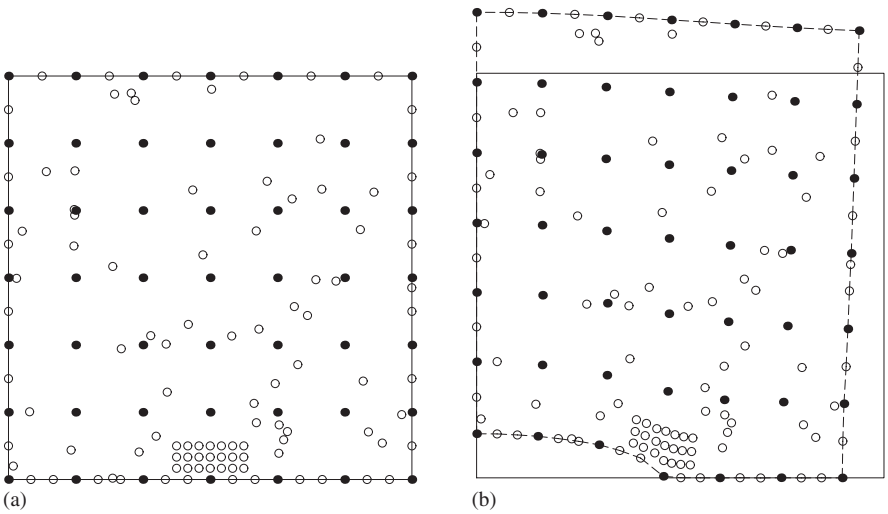

Figure 5. (a) Locations of primary (filled circles) and secondary (empty circles) nodes in the quarter of a cracked plate, and (b) undeformed (solid line), deformed (dotted line) shape of the cracked plate, and final locations of primary and secondary nodes.

For the linear elastic problem the exact value J_L of the J-integral is given by (see, for example, [42]):

$$J_L = c\pi(1.325)^2 \frac{1-\nu^2}{E}\sigma_0^2$$

where $2c$ is the crack length; it equals 1 in the present case. In Figure 6(a), we exhibit the J-integrals computed for the linear and the non-linear elastic problems. A similar problem has been studied in [49] under plane stress conditions, and similar variations of the J-integral for the linear and non-linear problems have been found.

As an additional test of the MLPG mixed formulation, we compute the J-integral for the linear elastic problem with the pure displacement formulation and the proposed mixed pressure–displacement formulation. With the pure displacement formulation, the error in the computed values of J is 71.3%, while when using the mixed formulation the error is only 1.14%.

Figure 6(b) exhibits the crack opening displacements computed using the MLPG mixed formulation and the commercial FE code ANSYS using the 8-node element PLANE183 and 1057 nodes with high concentration at the crack tip. The good agreement between the two numerical solutions further validates the present mixed formulation. We note that the proposed MLPG mixed formulation requires only 168 nodes as compared with 1057 nodes with the FE method.

Figure 7(a) reports the concentration of the first Piola–Kirchhoff stress, defined as P_{22}/σ_0 for different values of the dead traction. It shows how the mixed formulation enhanced by secondary nodes is able to capture the stress concentration without leading to spurious oscillatory behaviors. From Figure 7(a) it can be concluded that increasing the tension in the plate decreases the order of singularity of the first Piola–Kirchhoff stress at the crack tip. Figure 7(b) reports instead the concentration of the axial Cauchy stress, defined as σ_{22}/σ_0 for different values of the dead traction. From Figure 7(b) it can be seen that increasing the tension in the plate enhances the order of

DOI: 10.1002/cnm

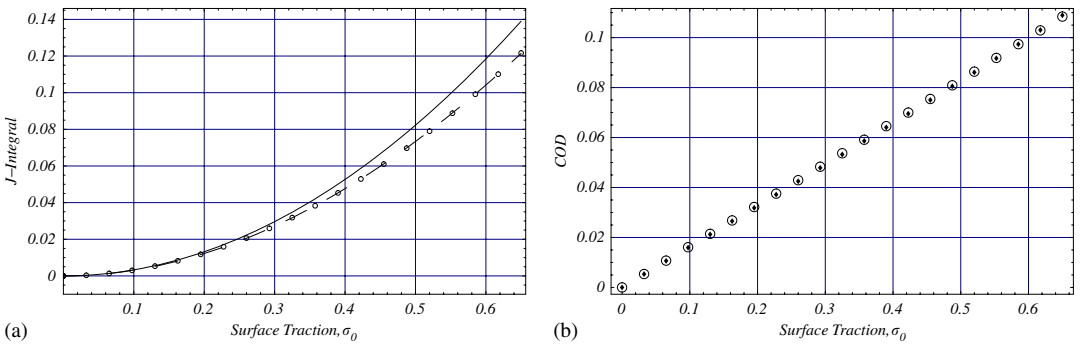

Figure 6. (a) J-integral from the linear analysis (solid curve) and J-integral from the non-linear analysis (empty circles and dashed fitting curve) *versus* applied nominal surface traction and (b) crack opening displacement computed using the MLPG formulation (diamond) and ANSYS FE code (empty circles) *versus* applied nominal surface traction.

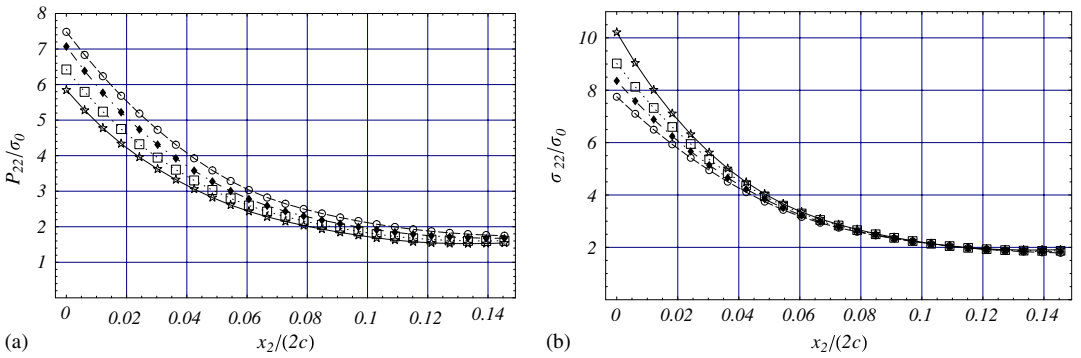

Figure 7. (a) Normalized first Piola–Kirchhoff stress in the neighborhood of the crack tip for different values of the applied nominal surface traction σ_0, and (b) normalized Cauchy stress in the neighborhood of the crack tip for different values of the applied nominal surface traction σ_0. In both figures, stars refer to the case of $\sigma_0 = 0.65$, squares to $\sigma_0 = 0.45$, diamonds to $\sigma_0 = 0.26$, and circles to $\sigma_0 = 0.065$.

singularity of the Cauchy stress at the crack tip. By comparing results in Figure 7(b) with those in Figure 7(a), one concludes that for a non-linear elastic problem the orders of singularity in the Cauchy stress and in the first Piola–Kirchhoff stress are different. For finite deformations these two stress tensors are different and are related by the deformation gradient.

Batra and Ching [50] have also delineated the differences in the energy release rates as Poisson's ratio is increased to $\frac{1}{2}$. The MLPG method has been employed in [51, 52] to analyze stresses near a crack tip in a plate loaded on the cracked side by surface tractions parallel to the crack. A transient linear elastodynamic problem for a cracked plate has been studied by the MSPH method in [53].

3.7. Remarks

When solving numerically boundary-value problems for incompressible materials by the FE method, one uses elements (equivalently basis functions for the trial solution and the test function)

DOI: 10.1002/cnm

that satisfy the Babuska–Brezzi condition [43]. In general, one needs to employ sophisticated analysis techniques to verify whether or not an element satisfies this condition. Hughes [16] has listed various FEs that do not satisfy this condition but still perform very well in the numerical solution of boundary-value problems for linear elastic incompressible materials. For non-linear boundary-value problems, the analysis becomes more involved, and the complexity increases further for the MLPG formulation. Even though we have not proved analytically that our choice of basis functions for the pressure and the displacement fields satisfies the Babuska–Brezzi condition, numerical experiments performed thus far and reported herein have indicated that these basis functions perform very well and do not exhibit the locking phenomenon for incompressible materials. It was proved in [36] that the MLPG formulation for 1-D linear elastic problems with Lagrange multipliers used to enforce essential boundary conditions satisfies the Babuska–Brezzi condition. In [46] the findings of [36] are extended to cracked beam problems.

Secondary nodes may be useful in those problems where stress concentrations or critical behaviors are expected in certain regions. Indeed, by adding secondary nodes the number of quadrature points needed for the numerical integration of the stiffness matrix and the load vector is not increased. Therefore, by adding secondary nodes one is able to increase the number of nodal degrees of freedom without noticeably increasing the computational time. Moreover, the use of a large number of secondary nodes may lead to ill-conditioned problems, since the basis functions of secondary nodes are not significantly different from those of primary nodes.

4. ANALYSIS OF PLANE STRESS PROBLEMS

For problems corresponding to the state of plane stress in the x_1x_2-plane,

$$\sigma_{13}=\sigma_{23}=\sigma_{33}=0$$

where $\boldsymbol{\sigma}$ is the Cauchy stress tensor. For a fully incompressible Mooney–Rivlin material,

$$\boldsymbol{\sigma}=-p\mathbf{1}+C_1\hat{\mathbf{B}}+C_2\hat{\mathbf{B}}^{-1}$$

where C_1 and C_2 are material parameters, $\hat{\mathbf{B}}$ is the left Cauchy–Green tensor, and p is the pressure that cannot be determined from the deformation field. The requirement $\sigma_{33}=0$ gives

$$p=C_1\hat{B}_{33}+C_2(\hat{\mathbf{B}}^{-1})_{33}$$

and the constitutive relation becomes

$$\boldsymbol{\sigma}=C_1(\hat{\mathbf{B}}-\hat{B}_{33}\mathbf{1})+C_2(\hat{\mathbf{B}}^{-1}-(\hat{\mathbf{B}}^{-1})_{33}\mathbf{1})$$

Thus, the boundary-value problem can be solved in the x_1x_2-plane for displacements w_1 and w_2 without solving for the pressure field. The displacement field $w_3(x_1, x_2)$ is computed from the isochoric condition $\det(\hat{\mathbf{B}})=1$ and the pressure field found from the equation given above. The procedure is illustrated in [49] and also in Section 5.11 of [54]. Thus, a pure displacement formulation in the x_1x_2-plane can be employed to study the plane stress problems for fully incompressible rubber-like materials.

DOI: 10.1002/cnm

5. CONCLUSIONS

We have studied finite plane strain deformations of a rubber-like material with the MLPG method, with the pressure and displacement fields treated as unknowns. Differing from the FE work, all variables are interpolated with the same set of MLS basis functions. By using Penn's invariants, the deformation is decomposed into a dilatation and a distortion, and consequently the strain energy is split into two parts: one depending only on dilatational strains and the other on distortional strains. In order to impose the essential boundary conditions, we consider an augmented formulation, where a set of Lagrange multipliers is defined on the relevant boundaries. A total Lagrangian formulation is derived and the resulting set of non-linear algebraic equations governing finite deformations is solved by Newton–Raphson's iterations.

A computer code has been developed and used to solve different problems. Computed results for a body made of a Mooney–Rivlin material under various loading conditions are shown to compare very well with either analytical solutions or numerical solutions obtained with a FE commercial code.

APPENDIX A: MLS BASIS FUNCTIONS

We present an MLS approximation technique based on the concept of primary and secondary nodes. The approach is similar to that presented in [42] with the main difference being that we do not require a background mesh. We use the traditional MLS approximation of [41] based on the Gaussian and the Spline weight functions for the generation of the entire set of trial functions, whereas in [42] the FE basis functions are used as weight functions for the primary nodes.

Consider a continuous scalar function q defined on the two-dimensional connected domain Ω. The generic point in Ω is indicated by $\mathbf{x}$ and its coordinates in a Cartesian coordinate system are x_1 and x_2. The (fictitious) nodal values at N scattered points $\mathscr{N}=\{\mathbf{x}_1,\mathbf{x}_2,\ldots,\mathbf{x}_N\}$ in $\bar{\Omega}$ are collected into the N-vector $\hat{\mathbf{q}}=[\hat{q}_1,\ldots,\hat{q}_N]^{\mathrm{T}}$. We partition the set of nodes into two subsets: the set of primary nodes $\mathscr{N}_{\mathrm{P}}$ and the set of secondary nodes $\mathscr{N}_{\mathrm{S}}$. The global approximation q^h of q in Ω is defined as

$$q(\mathbf{x})\simeq q^h(\mathbf{x})=\mathbf{p}^{\mathrm{T}}(\mathbf{x})\mathbf{a}(\mathbf{x}),\quad \mathbf{x}\in\Omega \tag{A1}$$

where

$$\mathbf{p}^{\mathrm{T}}(\mathbf{x})=[p_1(\mathbf{x}),p_2(\mathbf{x}),\ldots,p_m(\mathbf{x})] \tag{A2}$$

is a complete monomial basis of order m. For example,

$$\mathbf{p}^{\mathrm{T}}(\mathbf{x})=[1,x_1,x_2]\quad \text{linear basis},\quad m=3$$

The m-vector $\mathbf{a}(\mathbf{x})=[a_1(\mathbf{x}),\ldots,a_m(\mathbf{x})]^{\mathrm{T}}$ is composed of indeterminate coefficients, which vary with the point $\mathbf{x}$ on the domain Ω. At each location $\bar{\mathbf{x}}$ in Ω these coefficients are determined by a local least-square approximation of $q(\mathbf{x})$ on a small neighborhood $\Omega_{\bar{\mathbf{x}}}$ of $\bar{\mathbf{x}}$. The local approximation $q_{\bar{\mathbf{x}}}(\mathbf{x})$ is defined by

$$q(\mathbf{x})\simeq q_{\bar{\mathbf{x}}}(\mathbf{x})=\mathbf{p}^{\mathrm{T}}(\mathbf{x})\mathbf{a}(\bar{\mathbf{x}}),\quad \mathbf{x}\in\Omega_{\bar{\mathbf{x}}}\subset\Omega \tag{A3}$$

DOI: 10.1002/cnm

Therefore, in a small neighborhood of a generic point $\bar{\mathbf{x}}$ the coefficients a_i are treated as the unknown constants of the classical polynomial least-square approximation, and they are determined by minimizing the following functional $J_{\bar{\mathbf{x}}}$ representing the weighted discrete L^2 error norm:

$$J_{\bar{\mathbf{x}}}(\mathbf{a}) = \sum_{i=1}^{N} W_i(\bar{\mathbf{x}})[q_{\bar{\mathbf{x}}}(\mathbf{x}_i) - \hat{q}_i]^2 \tag{A4}$$

The function W_i is the weight function of node i.

At a given location $\bar{\mathbf{x}}$ only few terms in the summation (A4) are not zero since the supports of the weight functions W_i are much smaller than the domain Ω. This reduces the memory allocations when implementing the algorithm in a computer code and strengthens the local character of the MLS approximation.

The functional $J_{\bar{\mathbf{x}}}$ may be rewritten in matrix notation as

$$J_{\bar{\mathbf{x}}}(\mathbf{a}) = (\mathbf{P}\mathbf{a} - \hat{\mathbf{q}})^{\mathrm{T}} \mathbf{W}(\bar{\mathbf{x}})(\mathbf{P}\mathbf{a} - \hat{\mathbf{q}})$$

where $\mathbf{P}$ is an (N, m) matrix of real numbers:

$$\mathbf{P}^{\mathrm{T}} = [\mathbf{p}^{\mathrm{T}}(\mathbf{x}_1) \quad \dots \quad \mathbf{p}^{\mathrm{T}}(\mathbf{x}_N)]$$

and $\mathbf{W}$ is the following (N, N) diagonal matrix:

$$\mathbf{W}(\bar{\mathbf{x}}) = \mathrm{Diag}[W_1(\bar{\mathbf{x}}) \quad \dots \quad W_N(\bar{\mathbf{x}})]$$

The stationarity of $J_{\bar{\mathbf{x}}}$ with respect to $\mathbf{a}$ yields

$$\mathbf{A}(\bar{\mathbf{x}})\mathbf{a}(\bar{\mathbf{x}}) = \mathbf{B}(\bar{\mathbf{x}})\hat{\mathbf{q}} \tag{A5}$$

where (m, m) and (m, N) matrices $\mathbf{A}$ and $\mathbf{B}$ are defined by

$$\mathbf{A}(\bar{\mathbf{x}}) = \mathbf{P}^{\mathrm{T}} \mathbf{W}(\bar{\mathbf{x}}) \mathbf{P}, \quad \mathbf{B}(\bar{\mathbf{x}}) = \mathbf{P}^{\mathrm{T}} \mathbf{W}(\bar{\mathbf{x}}) \tag{A6}$$

We note that matrices $\mathbf{A}$ and $\mathbf{B}$ depend on the spatial coordinate $\bar{\mathbf{x}}$ only through the weight functions, since $\mathbf{P}$ is a matrix of real numbers. Solving for $\mathbf{a}$ in Equation (A5) and substituting the result in the global approximation (A3) we obtain the MLS approximation

$$q^h(\mathbf{x}) = \mathbf{p}^{\mathrm{T}}(\mathbf{x}) \mathbf{A}^{-1}(\mathbf{x}) \mathbf{B}(\mathbf{x}) \hat{\mathbf{q}} \tag{A7}$$

which, upon introducing the basis functions $\boldsymbol{\psi}(\mathbf{x})$, can be expressed as

$$q^h(\mathbf{x}) = \boldsymbol{\psi}^{\mathrm{T}}(\mathbf{x}) \hat{\mathbf{q}}, \quad \boldsymbol{\psi} = [\psi_1 \quad \dots \quad \psi_N]^{\mathrm{T}}, \quad \boldsymbol{\psi}^{\mathrm{T}}(\mathbf{x}) = \mathbf{p}^{\mathrm{T}}(\mathbf{x}) \mathbf{A}^{-1}(\mathbf{x}) \mathbf{B}(\mathbf{x}) \tag{A8}$$

For node $\mathbf{x}_i$,

$$q^h(\mathbf{x}_i) \neq \hat{q}_i$$

That is, the value of the approximating function at a node does not equal, in general, the value at that node of the function. Said differently, $\psi_j(\mathbf{x}_i) \neq \delta_{ij}$, where δ_{ij} is the Kronecker delta.

DOI: 10.1002/cnm

For primary nodes we use Gaussian weight functions with square supports:

$$W_i(\mathbf{x})=\begin{cases}\left(\exp\left[-\left(\dfrac{x_1-x_{i1}}{c_i}\right)^{2k}\right]-\exp\left[-\left(\dfrac{r_i}{c_i}\right)^{2k}\right]\right)\Big/\left(1-\exp\left[-\left(\dfrac{r_i}{c_i}\right)^{2k}\right]\right)\\ \quad\times\left(\exp\left[-\left(\dfrac{x_2-x_{i2}}{c_i}\right)^{2k}\right]-\exp\left[-\left(\dfrac{r_i}{c_i}\right)^{2k}\right]\right)\Big/\left(1-\exp\left[-\left(\dfrac{r_i}{c_i}\right)^{2k}\right]\right), \quad 0\leqslant|x_1-x_{i1}|,|x_2-x_{i2}|\leqslant r_i\\ 0, \quad |x_1-x_{i1}|,|x_2-x_{i2}|>r_i\end{cases} \tag{A9}$$

where c_i and k are constants controlling the shape of the weight function, and r_i is the length of the side of the square support. Each secondary node $\mathbf{x}_i\in\mathcal{N}_S$ is associated with its closest primary node $\bar{\imath}$, $\mathbf{x}_{\bar{\imath}}\in\mathcal{N}_P$, and its weight function is the product of $W_{\bar{\imath}}(x)$ and $\tilde{W}_{\bar{\imath}}(x)$ defined by

$$\tilde{W}_i(\mathbf{x})=\begin{cases}\left(1-6\left(\dfrac{x_1-x_{i1}}{\tilde{r}_i}\right)^2+8\left(\dfrac{x_1-x_{i1}}{\tilde{r}_i}\right)^3-3\left(\dfrac{x_1-x_{i1}}{\tilde{r}_i}\right)^4\right)\\ \quad\times\left(1-6\left(\dfrac{x_2-x_{i2}}{\tilde{r}_i}\right)^2+8\left(\dfrac{x_2-x_{i2}}{\tilde{r}_i}\right)^3-3\left(\dfrac{x_2-x_{i2}}{\tilde{r}_i}\right)^4\right), \quad 0\leqslant|x_1-x_{i1}|,|x_2-x_{i2}|\leqslant\tilde{r}_i\\ 0, \quad |x_1-x_{i1}|,|x_2-x_{i2}|>\tilde{r}_i\end{cases} \tag{A10}$$

where $\tilde{r}_i$ is a constant controlling the support of the weight function. Therefore, once a secondary node is placed in the domain it is associated with the closest primary node and that primary node determines the shape of its weight function. Thus, the support of the weight function of a secondary node is included in the support of the weight function of the corresponding primary node. In this way the number of quadrature points used in the numerical evaluation of matrices and vectors in the discrete formulation (13) is only dictated by the number of primary nodes and supports of their weight functions. Hence, integrals in (13) can be computed by adding integrals on the partitions of the domain generated by intersecting the supports of the weight functions of the primary nodes.

APPENDIX B: HYPERELASTIC AND MOONEY–RIVLIN MATERIALS

For an isotropic hyperelastic material, the strain energy density (per unit volume in the reference configuration) function can be expressed as

$$W(\mathbf{F})=W(I_1,I_2,I_3)$$

where I_1, I_2, and I_3 are principal invariants of the right Cauchy–Green strain tensor $\mathbf{C}$. From the strain energy function, one obtains the following expression for the second Piola–Kirchhoff stress tensor:

$$\mathbf{S}=2\frac{\partial W}{\partial I_1}\mathbf{1}+2\frac{\partial W}{\partial I_2}(I_1\mathbf{1}-\mathbf{C})+2\frac{\partial W}{\partial I_3}I_3\mathbf{C}^{-1}$$

DOI: 10.1002/cnm

For incompressible materials the deformation gradient must satisfy the constraint

$$\det \mathbf{F} = J = 1 \tag{B1}$$

at each point of the body. Because of the constraint (B1) derivatives of the strain energy density with respect to the three principal invariants are not independent, and the strain energy density is modified as follows to accommodate the constraint:

$$W(I_1, I_2) + p(J-1)$$

where p is called pressure, and it cannot be determined from the deformation of the body. Hence, for the stress tensor we have

$$\mathbf{S} = 2\left(\frac{\partial W}{\partial I_1}\frac{\partial I_1}{\partial \mathbf{C}} + \frac{\partial W}{\partial I_2}\frac{\partial I_2}{\partial \mathbf{C}}\right) + p\mathbf{C}^{-1}$$

For nearly incompressible isotropic hyperelastic materials, the stored energy function may be expressed as (see, e.g. [43])

$$W(\mathbf{C}, p) = \bar{W}(\mathbf{C}) + Q(\mathbf{C}, p) \tag{B2}$$

where

$$J_1 = I_1 (I_3)^{-1/3}, \quad J_2 = I_2 (I_3)^{-2/3}$$

and

$$\bar{W}(\mathbf{C}) = W_1(J_1, J_2) + W_2(J), \quad W_2(J) = kG(J)$$

$$Q(\mathbf{C}, p) = -\frac{1}{2k}(\bar{p}(J) - p)^2, \quad \bar{p} = -\frac{\mathrm{d}W_2}{\mathrm{d}J} = -k\frac{\mathrm{d}G}{\mathrm{d}J}$$

Here, W_1 and W_2 are the strain energy densities depending on the distortional and dilatational deformations, respectively; k describes the degree of compressibility; the function G vanishes only for isochoric deformations, and $\bar{p}$ is the pressure computed from the deformation gradient. Formally, when $k \to \infty$ the material becomes incompressible. The parameters J_1 and J_2 are the reduced invariants proposed in [4] to separate the deformation into distortional and dilatational parts. Following this decomposition, the second Piola–Kirchhoff stress tensor is expressed as

$$\mathbf{S} = 2\frac{\partial W}{\partial \mathbf{C}} = 2\left(\frac{\partial \bar{W}}{\partial \mathbf{C}} + \frac{\partial Q}{\partial \mathbf{C}}\right) = \bar{\mathbf{S}} - \frac{2}{k}(\bar{p} - p)\frac{\partial \bar{p}}{\partial \mathbf{C}}, \quad \bar{\mathbf{S}} = 2\frac{\partial \bar{W}}{\partial \mathbf{C}}$$

The contribution to the stress field from displacements may be rewritten as

$$\bar{\mathbf{S}} = 2\left(\frac{\partial W_1}{\partial J_1}\frac{\partial J_1}{\partial \mathbf{C}} + \frac{\partial W_2}{\partial J_2}\frac{\partial J_2}{\partial \mathbf{C}} - \bar{p}\frac{\partial J}{\partial \mathbf{C}}\right)$$

By computing the derivatives of the reduced invariants with respect to the strain tensor and by introducing the quantities,

$$K_1 = \frac{\partial W_1}{\partial J_1}, \quad K_2 = \frac{\partial W_1}{\partial J_2}$$

DOI: 10.1002/cnm

the tensor $\bar{\mathbf{S}}$ becomes

$$\bar{\mathbf{S}}=2\left(K_1 I_3^{-1/3}\left(\mathbf{I}-\frac{1}{3}I_1\mathbf{C}^{-1}\right)+K_2 I_3^{-2/3}\left(I_1\mathbf{I}-\mathbf{C}-\frac{2}{3}I_2\mathbf{C}^{-1}\right)\right)-J\bar{p}\mathbf{C}^{-1}$$

where we used the relations

$$\frac{\partial I_1}{\partial \mathbf{C}}=\mathbf{I},\quad \frac{\partial I_2}{\partial \mathbf{C}}=I_1\mathbf{I}-\mathbf{C},\quad \frac{\partial I_3}{\partial \mathbf{C}}=I_3\mathbf{C}^{-1}$$

For nearly incompressible materials, several forms of the strain energy function are available in the literature, see, e.g. [12]. Following [21] we use

$$W_1=\sum_{m+n=1}^{\infty}A_{mn}(J_1-3)^m(J_2-3)^n \tag{B3}$$

$$G=\tfrac{1}{2}(J-1)^2 \tag{B4}$$

Expression (B4) for the dilatation energy was proposed in [55]. We note that the resulting pressure field is given by

$$\bar{p}=-\frac{\mathrm{d}W_2}{\mathrm{d}J}=-k(J-1)$$

For Mooney–Rivlin materials

$$W_1=A_{10}(J_1-3)+A_{01}(J_2-3) \tag{B5}$$

Henceforth, we obtain

$$K_1=A_{10},\quad K_2=A_{01}$$

The choice of the dilatational strain energy is somewhat non-unique, since it has not been proved so far that it allows for the convergence of the solution for a nearly incompressible body to the solution of the corresponding compressible one, but numerical experiments (see, e.g. [21]) have shown its efficacy.

For the dilatation energy function (B4), the stress tensor is given by

$$\mathbf{S}=2\left(K_1 I_3^{-1/3}\left(\mathbf{I}-\frac{1}{3}I_1\mathbf{C}^{-1}\right)+K_2 I_3^{-2/3}\left(I_1\mathbf{I}-\mathbf{C}-\frac{2}{3}I_2\mathbf{C}^{-1}\right)\right)-pJ\mathbf{C}^{-1}$$

We note that in this formulation the incompressibility constraint is imposed by increasing the value of the parameter k. The approach is equivalent to the one followed in the linear elastic case when the Poisson ratio was chosen close to $\frac{1}{2}$.

The elasticity tensor $\mathbb{C}$ has the following expression:

$$\mathbb{C}=2\frac{\partial \mathbf{S}}{\partial \mathbf{C}}=\frac{4}{3}K_1 I_3^{-1/3}\left[-2\mathbf{C}^{-1}\boxtimes\mathbf{I}+\frac{1}{3}I_1[\mathbf{C}^{-1}\otimes\mathbf{C}^{-1}+3\mathbf{C}^{-1}\odot\mathbf{C}^{-1}]\right]$$
$$+\frac{4}{3}K_2 I_3^{-2/3}\left[-4I_1\mathbf{C}^{-1}\boxtimes\mathbf{I}+4\mathbf{C}^{-1}\boxtimes\mathbf{C}^{-1}+2I_2\left(\frac{2}{3}\mathbf{C}\otimes\mathbf{C}^{-1}+\mathbf{C}^{-1}\odot\mathbf{C}^{-1}\right)+3(\mathbf{I}\otimes\mathbf{I}-\mathbf{I}\odot\mathbf{I})\right]$$

DOI: 10.1002/cnm

$$+4H_{11}I_3^{-2/3}\left(\mathbf{I}-\frac{1}{3}I_1\mathbf{C}^{-1}\right)\otimes\left(\mathbf{I}-\frac{1}{3}I_1\mathbf{C}^{-1}\right)+4H_{12}\left[\left(\mathbf{I}-\frac{1}{3}I_1\mathbf{C}^{-1}\right)\otimes\left(I_1\mathbf{I}-\mathbf{C}-\frac{2}{3}I_2\mathbf{C}^{-1}\right)\right]$$

$$+4H_{22}I_3^{-4/3}\left(I_1\mathbf{I}-\mathbf{C}-\frac{2}{3}I_2\mathbf{C}^{-1}\right)\otimes\left(I_1\mathbf{I}-\mathbf{C}-\frac{2}{3}I_2\mathbf{C}^{-1}\right)-pJ(\mathbf{C}^{-1}\otimes\mathbf{C}^{-1}-2\mathbf{C}^{-1}\odot\mathbf{C}^{-1})$$

with (in Cartesian coordinates)

$$H_{ij}=\frac{\partial W_1}{\partial J_i\partial J_j},\quad \mathbf{A}\boxtimes\mathbf{B}=\tfrac{1}{2}(\mathbf{A}\otimes\mathbf{B}+\mathbf{B}\otimes\mathbf{A}),\quad (\mathbf{A}\odot\mathbf{A})_{ijkl}=\tfrac{1}{2}(A_{ik}A_{jl}+A_{il}A_{jk})$$

and

$$\frac{\partial\mathbf{C}^{-1}}{\partial\mathbf{C}}=-\mathbf{C}^{-1}\odot\mathbf{C}^{-1}$$

Similarly, the tensor $\mathbf{H}$ relating the incremental stress to the incremental pressure and the tensor $\mathbf{Q}$ are given by

$$\mathbf{H}=\frac{\partial\mathbf{S}}{\partial p}=-J\mathbf{C}^{-1},\quad \mathbf{Q}=2\frac{\partial\bar{p}}{\partial\mathbf{C}}=-kJ\mathbf{C}^{-1}\equiv k\mathbf{H}$$

Expressions for tensors $\mathbb{C}$, $\mathbf{H}$, and $\mathbf{Q}$ for a natural reference configuration are

$$\mathbb{C}=\tfrac{4}{3}(K_1+K_2)(3\mathbf{I}\odot\mathbf{I}-\mathbf{I}\otimes\mathbf{I}),\quad \mathbf{H}=-\mathbf{I},\quad \mathbf{Q}=-k\mathbf{I}$$

Therefore, for infinitesimal deformations the material behaves as an isotropic linear elastic with constitutive parameters

$$v=\frac{1}{2}\left(1-2\frac{K_1+K_2}{k}\right),\quad E=\left(6-4\frac{K_1+K_2}{k}\right)(K_1+K_2)$$

REFERENCES

1. Nagdi K. *Rubber as an Engineering Material*: *Guidelines for Users*. Hanser: New York, 1993.
2. Ogden RW. *Nonlinear Elasticity with Application to Material Modeling*. Lecture Notes 6 in IPPTPAN, Warsaw, Poland, 2003.
3. Saccomandi G. In *Universal Results in Finite Elasticity. Non-linear Elasticity*, Fu Y, Ogden R (eds). Cambridge University Press: Cambridge, 2001.
4. Penn R-W. Volume changes accompanying the extension of rubber. *Journal of Rheology* 1970; **4**:509–517.
5. Crisfield MA. Non-linear finite element analysis of solids and structures. *Advanced Topics*, vol. 2. Wiley: Chichester, 1998.
6. Charrier P, Dacorogna B, Hanouzet B, Laborde P. An existence theorem for slightly incompressible materials in non linear elasticity. *SIAM Journal on Mathematical Analysis* 1998; **19**:70–85.
7. Reissner E, Atluri SN. On the formulation of variational theorems involving volume constraints. *Computational Mechanics* 1989; **5**:337–344.
8. Gadala MS. Numerical solution of non-linear problems of continua-I, survey of incompressibility constraints and software aspects. *Computers and Structures* 1986; **22**:841–855.
9. Mackerle L. Rubber and rubber-like materials, finite-element analyses and simulations, an addendum: a bibliography (1997–2003). *Modelling and Simulation in Materials Science and Engineering* 2004; **12**:1031–1053.
10. Hermann LR. Elasticity equations for incompressible and nearly incompressible materials by variational theorem. *AIAA Journal* 1965; **3**:1896–1900.

DOI: 10.1002/cnm

11. Batra RC. Finite plane strain deformation of rubberlike materials. *International Journal for Numerical Methods in Engineering* 1980; **15**:145–160.
12. Peng SH, Chang W. A compressible approach in finite element analysis of rubber-elastic materials. *Computers and Structures* 1997; **62**:573–593.
13. Scharnost T, Pian THH. Finite element analysis of rubber-like materials by a mixed model. *International Journal for Numerical Methods in Engineering* 1978; **12**:665–676.
14. Murakawa H, Atluri SN. Finite elasticity solutions using hybrid finite elements based on a complementary energy principle—Part II: incompressible materials. *Journal of Applied Mechanics* (ASME) 1979; **70-APM-6**:71–78.
15. Seki W, Atluri SN. Analysis of strain localization in hyperelastic strain-softening materials using hybrid-stress finite elements with drilling degrees of freedom. *Computational Mechanics* 1994; **14**:549–585.
16. Hughes TJR. *The Finite Element Method. Linear Static and Dynamic Finite Element Analysis*. Prentice-Hall: Englewood Cliffs, NJ, 1987.
17. Chen JS, Han W, Tu CT, Duan W. On the perturbed Lagrangian for nearly incompressible and incompressible hyperelasticity. *Computer Methods in Applied Mechanics and Engineering* 1997; **142**:335–351.
18. Chen JS, Pan C, Chang TYP. On the control of pressure oscillations in bilinear-displacements constant-pressure elements. *Computer Methods in Applied Mechanics and Engineering* 1995; **128**:137–152.
19. Belytschko T, Lu YY, Gu L. Element-free Galerkin methods. *International Journal for Numerical Methods in Engineering* 1994; **37**:229–256.
20. Duarte CAM, Oden JT. Hp clouds—an hp meshless method. *Numerical Methods for Partial Differential Equations* 1996; **12**:673–705.
21. Chen JS, Pan C, Wu CT. Large deformation of rubber based on a reproducing kernel particle method. *Computational Mechanics* 1997; **19**:211–227.
22. Lucy LB. A numerical approach to the testing of the fission hypothesis. *The Astronomical Journal* 1977; **82**:1013–1024.
23. Nayroles B, Touzot G, Villon P. Generalizing the finite element method: diffuse approximation and diffuse elements. *Computational Mechanics* 1992; **10**:307–318.
24. Melenk JM, Babuska I. The partition of unity finite element method: basic theory and applications. *Computer Methods in Applied Mechanics and Engineering* 1996; **139**:289–314.
25. Sukumar N, Moran B, Belytschko T. The natural element method in solid mechanics. *International Journal for Numerical Methods in Engineering* 1998; **43**:839–887.
26. Wendland H. Piecewise polynomial, positive definite and compactly supported radial basis functions of minimal degree. *Advances in Computational Mathematics* 1995; **4**:389–396.
27. Atluri SN, Zhu T. A new Meshless Local Petrov–Galerkin (MLPG) approach in computational mechanics. *Computational Mechanics* 1998; **22**:2117–2127.
28. Zhang GM, Batra RC. Modified smoothed particle hydrodynamics method and its application to transient problems. *Computational Mechanics* 2004; **34**:137–146.
29. Ferreira AJM, Batra RC, Roque CMC, Qian LF, Martins PALS. Static analysis of functionally graded plates using third-order shear deformation theory and a meshless method. *Composite Structures* 2005; **69**:449–457.
30. Atluri SN, Shen S. The meshless local Petrov–Galerkin (MLPG) method: a simple & less-costly alternative to finite element and boundary element methods. *Computer Modeling in Engineering and Sciences* 2002; **3**:11–51.
31. Gu YT, Liu GR. A meshless local Petrov–Galerkin (MLPG) method for free and forced vibration analyses for solids. *Computational Mechanics* 2001; **27**:188–198.
32. Gu YT, Liu GR. A meshless local Petrov–Galerkin (MLPG) formulation for static and free vibration analysis of thin plates. *Computer Modeling in Engineering and Sciences* 2001; **2**:463–476.
33. Atluri SN, Cho JY, Kim H-G. Analysis of thin beams, using the meshless local Petrov–Galerkin method, with generalized moving least squares interpolations. *Computational Mechanics* 1999; **24**:334–347.
34. Qian LF, Batra RC, Chen LM. Static and dynamic deformations of thick functionally graded elastic plates by using a higher-order shear and normal deformable plate theory and meshless local Petrov–Galerkin method. *Composites Part B* 2004; **35**:686–697.
35. Qian LF, Batra RC. Transient thermoelastic deformations of a thick functionally graded plate. *Journal of Thermal Stresses* 2004; **27**:705–740.
36. Batra RC, Porfiri M, Spinello D. Free and forced vibrations of a segmented bar by a meshless local Petrov–Galerkin (MLPG) formulation. *Computational Mechanics* 2007; DOI: 10.1007/s00466-006-0049-6.
37. Batra RC, Porfiri M, Spinello D. Electromechanical model of electrically actuated narrow microbeams. *Journal of Microelectromechanical Systems* 2006; **15**:1175–1189.

DOI: 10.1002/cnm

38. Batra RC, Porfiri M, Spinello D. Analysis of electrostatic MEMS using meshless local Petrov–Galerkin (MLPG) method. *Engineering Analysis with Boundary Elements* 2006; **30**:949–962.
39. Han ZD, Liu HT, Rajendran AM, Atluri SN. The applications of meshless local Petrov–Galerkin (MLPG) approaches in high-speed impact, penetration and perforation problems. *Computer Modeling in Engineering and Sciences* 2006; **14**:119–128.
40. Han ZD, Rajendran AM, Atluri SN. Meshless local Petrov–Galerkin (MLPG) approaches for solving nonlinear problems with large deformations and rotations. *Computer Modeling in Engineering and Sciences* 2005; **10**:1–12.
41. Lancaster P, Salkauskas K. Surfaces generated by moving least squares methods. *Mathematics of Computation* 1981; **37**:141–158.
42. Kim HG, Atluri SN. Arbitrary placement of secondary nodes, and error control, in the meshless local Petrov–Galerkin (MLPG) method. *Computer Modeling in Engineering and Sciences* 2000; **1**:11–32.
43. Bathe K-J. *Finite Element Procedures in Engineering Analysis*. Prentice-Hall: Englewood Cliffs, NJ, 1982.
44. Simo JC, Hughes JRT. *Computational Inelasticity*. Springer: New York, 1998.
45. Batra RC, Zhang GM. SSPH Basis functions for meshless methods, and comparison of solutions with strong and weak formulations. *Computational Mechanics* 2007; DOI: 10.1007/s00466-007-0209-3.
46. Andreaus U, Batra RC, Porfiri M. Vibrations of cracked Euler–Bernoulli beams using meshless local Petrov–Galerkin (MLPG) method. *Computer Modeling in Engineering and Sciences* 2005; **9**:111–131.
47. Batra RC, Liang XQ. Finite dynamic deformations of smart structures. *Computational Mechanics* 1997; **20**: 427–438.
48. Timoshenko SP, Goodier JN. *Theory of Elasticity* (3rd edn). McGraw-Hill: New York, 1970.
49. Legrain G, Moes N, Verron E. Stress analysis around crack tips in finite strain problems using the extended finite element method. *International Journal for Numerical Methods in Engineering* 2005; **63**:290–314.
50. Batra RC, Ching H-K. Comparison of energy release rates in a constrained epoxy disc with Hookean and Mooney–Rivlin materials. *Theoretical and Applied Fracture Mechanics* 2002; **38**:165–175.
51. Ching H-K, Batra RC. Determination of crack tip fields in linear elastostatics by the meshless local Petrov–Galerkin (MLPG) method. *Computer Modeling in Engineering and Sciences* 2001; **2**:273–289.
52. Batra RC, Ching H-K. Analysis of elastodynamic deformations near a crack–notch tip by the meshless local Petrov–Galerkin (MLPG) method. *Computer Modeling in Engineering and Sciences* 2002; **3**:717–730.
53. Batra RC, Zhang GM. Search algorithm and simulation of elastodynamic crack propagation by modified smoothed particle hydrodynamics (MSPH) method. *Computational Mechanics* 2007; **40**:531–546.
54. Batra RC. *Elements of Continuum Mechanics*. AIAA: Vienna, 2005.
55. Rivlin RS. Large elastic deformations of isotropic materials IV, further developments of general theory. *Philosophical Transactions of the Royal Society of London Series A* 1948; 379–397.

DOI: 10.1002/cnm